



Hybrid nanocomposites of tunneled-mesoporous sulfur-doped carbon nanofibers embedded with zinc sulfide nanoparticles for ultrafast lithium storage capability



Ki-Wook Sung ^{a,1}, Bon-Ryul Koo ^{b,1}, Hyo-Jin Ahn ^{a,b,*}

^a Department of Materials Science and Engineering, Seoul National University of Science and Technology, Seoul, 01811, South Korea

^b Program of Materials Science & Engineering, Convergence Institute of Biomedical Engineering and Biomaterials, Seoul National University of Science and Technology, Seoul, 01811, South Korea

ARTICLE INFO

Article history:

Received 3 August 2020

Received in revised form

11 September 2020

Accepted 14 September 2020

Available online 17 September 2020

Keywords:

Li-ion battery

Ultrafast lithium storage capability

Hybrid nanocomposite

Mesoporous carbon nanofiber

ZnS nanoparticle

ABSTRACT

As effective and simple approach by which to construct hybrid nanocomposite using ZnS nanoparticles (NPs) and conducting carbon materials to realize robust ultrafast lithium storage capabilities, we newly developed tunneled-mesoporous S-doped carbon nanofibers (SCNF) embedded with ZnS NPs through a one-pot carbonization process via the thiourea effect. This hybrid nanocomposite is unique given its tunneled-mesoporous CNF structure with well-dispersed ZnS NPs by ZnO sulfurization, offering available space to accept abrupt structural expansions of ZnS NPs and efficient Li-ion pathways during the electrochemical reaction. Using this material leads to competitive cycling stability and superior rate capabilities. Even at a high current density of 2000 mA g⁻¹, amazing ultrafast electrochemical performance outcomes with a high specific capacity (391.8 mAh g⁻¹) and good long-term cycling stability (97.2%) after 500 cycles were noted. These findings are attributed to the synergistic effects of the accelerated the transportation of Li ions for the ZnS NPs by the internal construction of the tunneled-mesoporous SCNF and facilitation of the electrical conductivity of the electrode via the S doping effect of the CNF matrix. Therefore, the proposed approach for a unique hybrid nanocomposite holds great potential regarding the development of an outstanding anode electrode to enhance the ultrafast lithium storage capabilities.

© 2020 Elsevier B.V. All rights reserved.

1. Introduction

Lithium-ion batteries (LIBs) have been recognized as a prominent power source for various portable electronic devices, such as smartphones and laptops, owing to notable characteristics such as a high energy density, good cycling stability, a low self-discharge rate, environmental friendliness, and little memory effect [1–5]. Commercially, the energy density of LIBs has reached 150 W h kg⁻¹; however, to use these devices in an electric vehicle intended to drive at least 300 miles per charge, the energy density of LIBs should be 300 W h kg⁻¹ [6,7]. Furthermore, given the recent large-scale utilization of LIBs, the exceptional specifications are now required, specifically greater increases in the rate capability and cycling stability as well as ultrafast capability [5,8]. To realize these

performances, the development of anode materials as alternatives to graphitic carbon and its low theoretical capacity of 372.0 mAh g⁻¹ is an important research objective because the anode electrodes in LIBs play a key role in enabling electric current in the system [9]. Among various alternative reported thus far, zinc sulfide (ZnS) has been considered as an ideal anode material due to its high theoretical capacity (962.0 mAh g⁻¹), high natural abundance, environmental friendliness, and facile synthesis methods [10]. However, practical lithium storage capabilities have been hindered by the inherently poor electrical conductivity and serious volume changes which occur during the Li-ion charge/discharge process, leading to extremely poor LIB performance outcomes stemming from the deteriorated structure and resultant electrode pulverization, which becomes even graver during ultrafast charging and discharging [10,11].

To overcome these limitations of ZnS, several strategies have been introduced in relation to accelerating the kinetics and stability of the electrode. An effective approach is nanosize the ZnS material [12–14]. This is useful to alleviate the structural expansion and

* Corresponding author. Department of Materials Science and Engineering, Seoul National University of Science and Technology, Seoul, 01811, South Korea.

E-mail address: hjahn@seoultech.ac.kr (H.-J. Ahn).

¹ K.-W. Sung and B.-R. Koo contributed equally to this work.

reduce the Li-ion diffusion length due to the increased specific surface area of this material. In addition, the unique nanostructuring of nanorods and nanosheets provides transmission paths for efficient Li-ion transportation, improving the cycling stability and rate performance of LIBs. A more advanced method relies on a composite of ZnS nanostructures with conducting carbon materials (amorphous carbon and reduced graphene oxide) [15,16]. Such carbon composites allow electrons and Li-ions to move quickly through the conductive carbon matrix in the vicinity of the ZnS nanostructures and, at the same time, relaxes the transformation of the nanostructures during repetitive charging/discharging. These factors are beneficial for improving the cycle and rate performances, but such values of the electrochemical behavior could be unfortunately lost under an ultrafast current rate during the large-scale utilization of LIBs in the form of rapidly degrading specific capacity and cycling retention values [9,17]. Recently, a few reports noted that the hybridization of porous carbon nanostructures having both a large surface area and rapid rates of electrical conductivity with ZnS is a promising strategy to realize approach satisfactory ultrafast lithium storage capability outcomes. Nevertheless, in these studies, a metal-organic framework (MOF) skeleton or a hard template was mostly commonly used, making the preparation of the hybrid nanostructures highly complex and expensive, with the resultant performances insufficient as well [18–20]. Therefore, developing desired hybrid nanostructures with ZnS and conductive porous carbon materials using a simple and effective process remains as a great challenge to be overcome before robust ultrafast LIB performances can be realized.

In this study, with the considerations above and to realize enhanced ultrafast LIB performances, we newly developed unique hybrid nanocomposites with tunneled-mesoporous S-doped carbon nanofibers (SCNF) and embedded ZnS nanoparticles (NPs) through a one-pot carbonization process via the thiourea effect. This approach involves the simple and effective construction of hybrid nanocomposites by means of original carbonization processes to accelerate the formation of tunneled mesopores and the S-doping effect in the CNF during the sulfurization of ZnO NPs by the thermal decomposition of thiourea. The hybrid nanocomposites have synergistic advantages that improve the electrochemical kinetics and stability, making them useful for ultrafast lithium storage by LIBs. That is, the tunneled-mesopore CNF structure not only reduces the Li-ion diffusion pathways for ZnS NPs but also provides available room for the extensive volume change of the ZnS NPs during the Li-ion charge/discharge process. Moreover, S-doping in the CNF can accelerate the electrical conductivity of the electrodes for efficient charge transportation in LIBs. With the combination of these unique features, the hybrid nanocomposites deliver stable rate capability and long-term cycling retention at an ultrafast current density (2000 mA/g) as high-performance anode electrodes for ultrafast LIBs.

2. Experimental

2.1. Chemicals

ZnO NPs (<50 nm in particle size), thiourea ($\text{CH}_4\text{N}_2\text{S}$, 99.0%), polyacrylonitrile (PAN, $M_w = 150,000$), and *N,N*-dimethylformamide (DMF, 99.8%) were purchased from Sigma-Aldrich. All chemicals were used without further purification.

2.2. Synthesis of hybrid nanocomposites

The hybrid nanocomposites with the tunneled-mesoporous SCNF embedded with ZnS NPs were successfully fabricated through electrospinning with a subsequent carbonization step. To

prepare the solution for the electrospinning step, 15 wt% ZnO NPs was dispersed in DMF dissolved with 10 wt% PAN, after which thiourea acting as a medium to induce the sulfurization of the ZnO NPs was dissolved in the PAN solution with the dispersed ZnO NPs, with the added amount of thiourea in the solution adjusted to 2, 3, and 4 wt% in order to optimized the construction of the hybrid nanocomposites. The electrospinning process was performed by applying voltage of 13 kV between a needle (23 gauge) and the Al collector at a distance of 15 cm and with the feeding rate of the syringe fixed at 0.03 mL h^{-1} . Additionally, ZnO NPs-embedded PAN nanofibers with different amounts of thiourea (2, 3, and 4 wt%) were stabilized at 280°C for 2 h in air and then calcined at 800°C for 2 h. Accordingly, three types of hybrid nanocomposites were obtained as a result of ZnO NPs sulfurization (herein referred to as ZnS/SCNF-T2, ZnS/SCNF-T3, and ZnS/SCNF-T4). For comparison, we prepared bare CNF through the carbonization of PAN nanofibers without thiourea.

2.3. Characterizations

Differential scanning calorimetry (DSC) measurements and a thermogravimetric analysis (TGA) were conducted at a heating rate of $10^\circ\text{C min}^{-1}$. The crystal structure was traced by X-ray diffraction analyses (XRD, Rigaku D/Max 2500V) between 10° and 80° with a step size of 0.02° . The structures and morphologies were examined by means of field-emission scanning electron microscopy (FESEM, Hitachi S-4800) and transmission electron microscopy (MULTI/TEM; Tecnai G², KBSI Gwangju Center). The element distribution was visualized by means of energy-dispersive spectrometry (EDS) mapping. The surface properties of the specific surface area, the pore volume, and the average pore diameter were investigated using the Brunauer–Emmett–Teller (BET) and Barrett–Joyner–Halenda (BJH) methods by obtaining the corresponding N_2 adsorption/desorption isotherms at 77 K. Chemical bonding states were analyzed by X-ray photoelectron spectroscopy (XPS, ESCALAB 250) using Al K_{α} X-ray sources. The electrical conductivity of the electrode was measured using a Hall effect measurement system (HMS-3000).

2.4. Electrochemical measurements

Electrochemical performances were measured using coin-type cells (CR2032, Hohsen Corporation) with the fabricated samples as the anode, a lithium metal foil (Honjo Chemical, 99.8%) as the counter electrode, a porous polypropylene membrane (Celgard 2400) as the separator, and a 1.0 M LiPF_6 solution in a mixture of dimethyl carbonate-ethylene carbonate (1:1) as the electrolyte. To fabricate the anode electrode, slurries were prepared by mixing 70 wt% of the prepared samples with 20 wt% of polyvinylidene fluoride (PVDF) as the binder and 10 wt% of Ketjenblack (Alfa Aesar) as the conducting material with *N*-methyl-2-pyrrolidinone. The homogenized slurries were coated using the doctor blade method onto a Cu foil (Nippon Foil, 18 mm) and then dried in an oven at 100°C for 12 h. The mass loading of the active materials on each electrode was about 15 mg. All coin-type cells were assembled in a high-purity argon-filled glove box (<5 ppm H_2O and O_2).

Charging/discharging tests were performed using a battery cyclor system (WonATech Corp., WMPG 3000) in the potential range of 0.05–3.00 V (vs. Li/Li^+) at 25°C in an incubator. Cyclic voltammetry (CV) measurements were carried out on a potentiostat/galvanostat (Eco Chemie Autolab PGST302 N) at a scan rate of 0.1 mV s^{-1} over the potential range of 0.05–3.00 V (vs. Li/Li^+). The cycling stability of the cells was evaluated up to 100 cycles at a current density of 100 mA g^{-1} . The rate performance outcome was examined at current densities of 100, 300, 700, 1000, 1500, and

2000 mA g⁻¹. The ultrafast cycling capability was examined for 500 cycles at a current density of 2000 mA g⁻¹. Electrochemical impedance spectroscopy (EIS) measurements were carried out using fresh cells over a frequency range of 10⁵–10⁻² Hz while applying an AC signal of 5 mV.

3. Results and discussion

Fig. 1a shows a schematic of the formation mechanism of the hybrid nanocomposites consisting of tunneled-mesoporous SCNF embedded with ZnS NPs using thiourea. During the carbonization process, the thiourea in the stabilized CNF with ZnO NPs (CNF/ZnO) acts as multi-functional media, causing mesopores and S-doping over the CNF as a result of the sulfurization of the ZnO NPs. Upon the initiation of the carbonization process, the thiourea can function as an H₂S source in the stabilized CNF/ZnO due to its thermal decomposition, producing H₂S, NH₃, CS₂, and HSCN gases, as confirmed by the relaxed exothermic peak in the temperature

range of 310–390 °C in the DSC curve compared to stabilized CNF without thiourea (see Fig. 1b) [21]. In particular, although the DSC curve of pristine thiourea shows decomposition reaction peak at a temperature lower than 310 °C, thiourea existing in the PAN fiber is observed at an increased decomposition temperature of 310–390 °C (Fig. S1). The sulfurization of the ZnO NPs embedded in the CNF by a chemical reaction with H₂S (ZnO + H₂S → ZnS + H₂O) then occurs at 480–610 °C, as indicated by the violent exothermic peak shown in the DSC curve [22,23]. At the same time, tunneled-mesopores in the CNF can arise due to an oxidation reaction (2H₂O + C → 2H₂ + CO₂) in the area surrounding the NPs induced by the formed H₂O, and the S doping of the CNF occurs due to the effect of the decomposed –SH molecules [24–26]. To clarify veracity of the multiple effects using thiourea, we used XRD (Fig. 1c) of ZnS/SCNF-T3 samples prepared at different carbonization temperatures of 400 and 600 °C in conjunction with the subsequent SEM results (Fig. S1). While there is no formation of tunneled mesopores for the 400 °C sample (Fig. S1a) as no triggering of

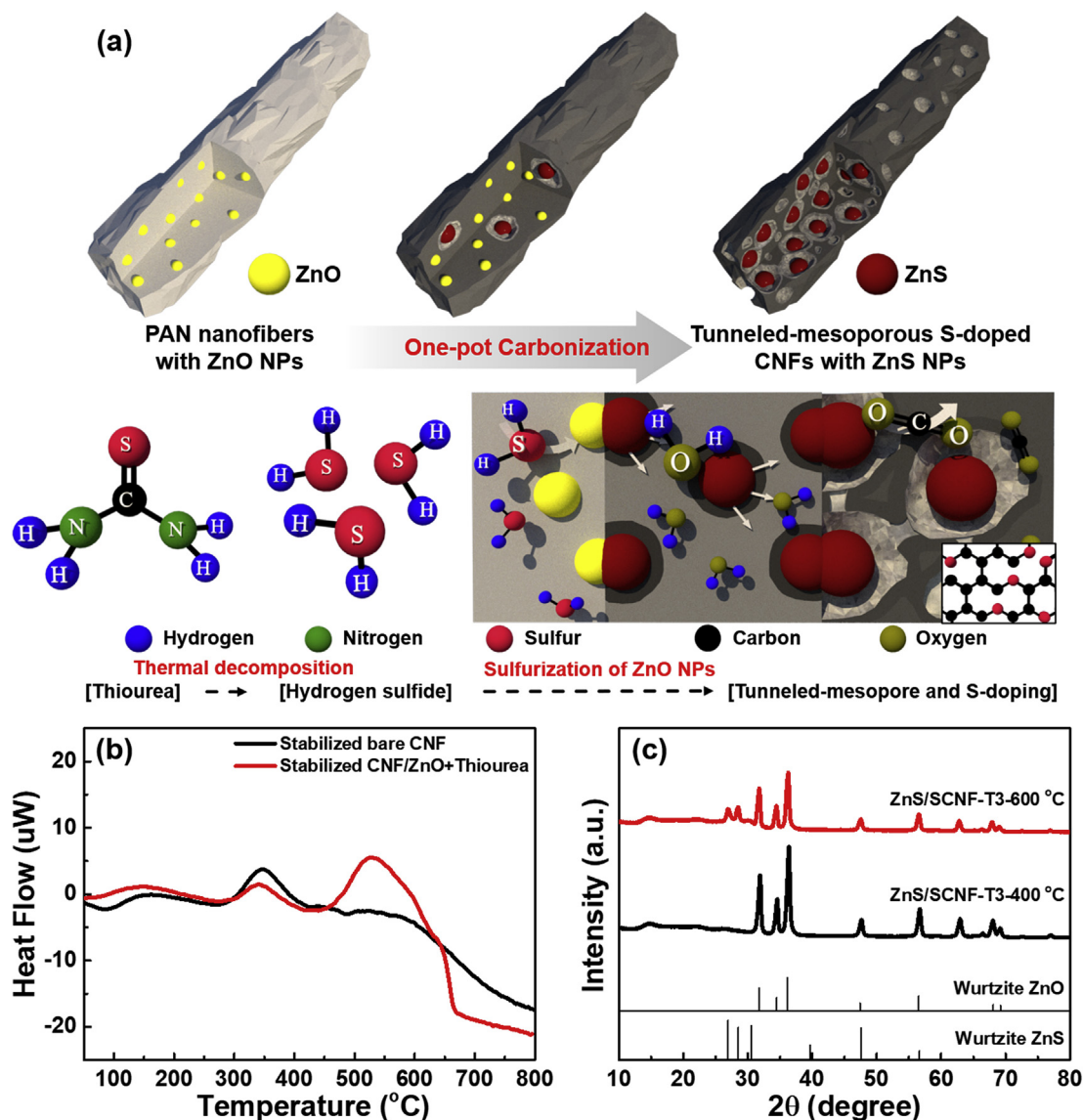


Fig. 1. (a) Schematic illustration of the formation mechanism of the hybrid nanocomposites consisting of tunneled mesoporous SCNF embedded with ZnS NPs by the thiourea effect, (b) DSC curves of stabilized bare CNF and stabilized CNF/ZnO samples with thiourea, and (c) XRD curves of ZnS/SCNF-T3 samples formed at different carbonization temperatures of 400 and 600 °C.

sulfurization occurred, the 600 °C sample (Fig. S1b) reveals the formation of partially tunneled mesopores in the CNF due to the presence of the ZnS, which was converted from ZnO. Therefore, it is expected that the thiourea in the CNF/ZnO can cause the formation of hybrid nanocomposites with tunneled-mesoporous SCNF and the embedded ZnS NPs by generating ZnO sulfurization to induce the tunneled mesopores and the S-doping in the CNF.

Fig. 2a–h display low-magnification and high-magnification FESEM images of the bare CNF, ZnS/SCNF-T2, ZnS/SCNF-T3, and ZnS/SCNF-T4 samples, respectively. In the low-magnification FESEM images shown in Fig. 2a–d, while the bare CNF sample has a dense and flat surface of a one-dimensional (1D) structure with a diameter range of approximately 116.01–136.43 nm, the surfaces of the ZnS/SCNF-T2, ZnS/SCNF-T3, and ZnS/SCNF-T4 samples appear to be uneven, together with increased diameters (~162.53–187.76 nm for ZnS/SCNF-T2, ~171.96–202.64 nm for ZnS/SCNF-T3, and ~175.69–438.94 nm for ZnS/SCNF-T4) in comparison to the bare CNF sample due to the deformation induced by the growth of the embedded NPs (~18.76–47.41 nm for ZnS/SCNF-T2, ~21.01–47.52 nm for ZnS/SCNF-T3, and ~26.5–81.79 nm for ZnS/SCNF-T4). Hence, the 1D structure of ZnS/SCNF-T4, showing excessive NP growth, became discontinuous, which can have negative effects on the electron transfer and the Li-ion diffusion

rate during the charge/discharge process [26]. Moreover, the high-magnification images shown in Fig. 2e–h clearly show the formation of tunneled mesopores inside of the uneven CNF, unlike the bare CNF sample with a dense cross-section. Interestingly, it was also found that the diameter of the formed tunneled mesopores and the corresponding distribution both gradually increase as the amount of thiourea used increases to 3 wt% while maintaining the 1D structure. This can be attributed to the oxidation reaction of the CNF induced by the growth of the NPs. That is, because using more thiourea can cause the gradual growth of ZnS NPs as a result of the recrystallization of ZnO to ZnS, the area of the CNF in contact with the embedded ZnS NPs to induce the oxidation reaction of the NPs increases, leading to the internal construction of the tunneled-mesoporous CNF structure. This unique structure improves the electrochemical performance by shortening the diffusion pathway of Li ions and providing available space for the volume expansion of the embedded ZnS NPs [27]. However, for the ZnS/SCNF-T4 sample, there is a discontinuous 1D structure as a result of the collapsed CNF induced by the excessive growth of the ZnS NPs located in it. The degree of the formation of the tunneled-mesoporous structure by the thiourea effect is clearly characterized by the BET measurements. As shown in the N₂ adsorption/desorption isotherms in Fig. 2i, while the bare CNF exhibits type I characteristics indicating

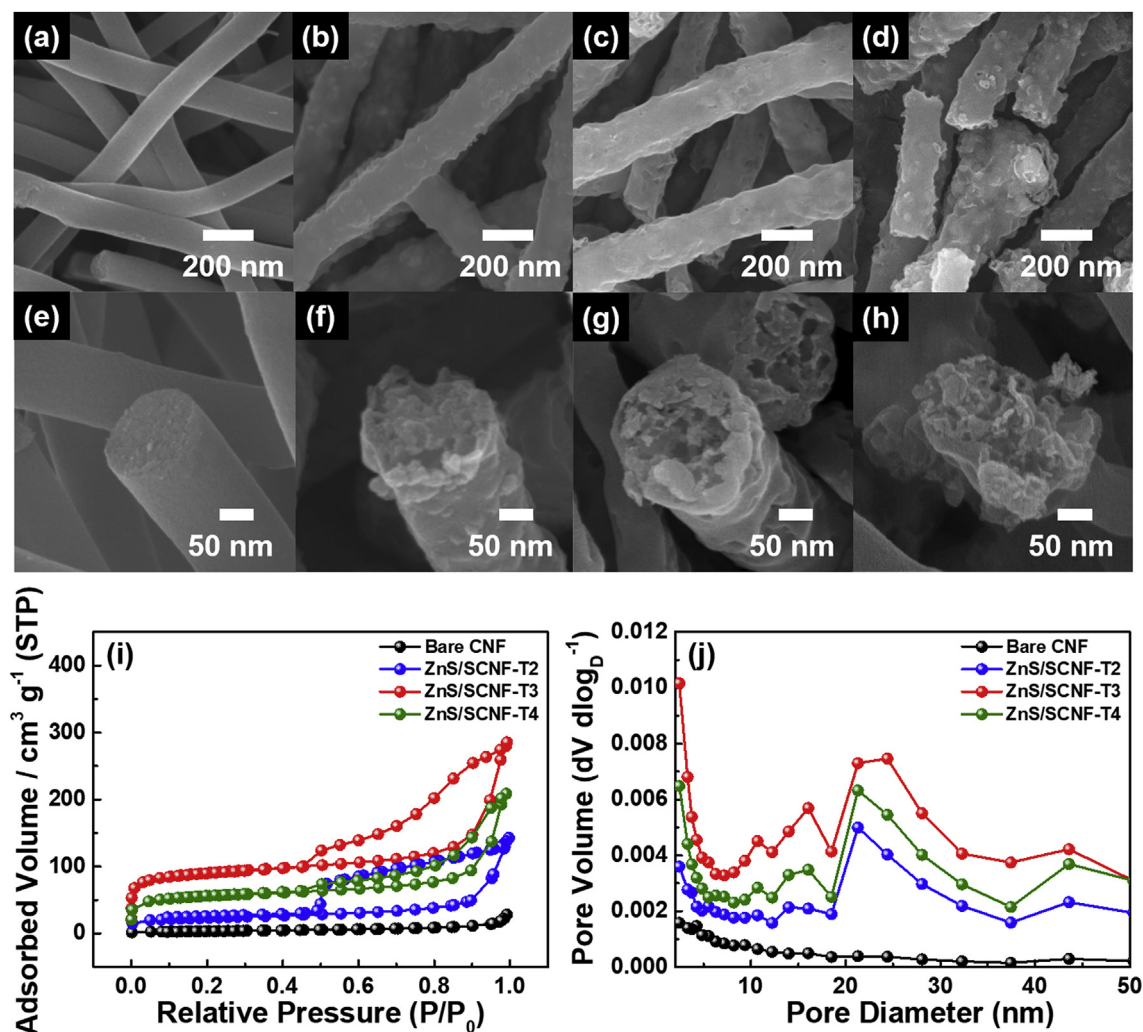


Fig. 2. (a–d) Low-magnification and (e–h) high-magnification SEM images of bare CNF, ZnS/SCNF-T2, ZnS/SCNF-T3, and ZnS/SCNF-T4, respectively, (i) N₂ adsorption/desorption isotherms, and (j) BJH pore size distribution.

the presence of micropores (pore diameter, < 2 nm), there are type IV characteristics related to the existence of mesopores (pore diameter, 2–50 nm) for the ZnS/SCNF samples [11,26]. By extension, in BJH measurements (see Fig. 2j), the tunneled-mesopore volume in the approximate range of 2.44–43.57 nm was found to increase from the bare CNF to the ZnS/SCNF-T3 sample but then decreases at ZnS/SCNF-T4, in good agreement with the SEM results, indicating that ZnS/SCNF-T3 has a higher specific surface area ($334.37 \text{ m}^2 \text{ g}^{-1}$) compared to the other samples ($31.37 \text{ m}^2 \text{ g}^{-1}$ for bare CNF, $82.68 \text{ m}^2 \text{ g}^{-1}$ for ZnS/SCNF-T2, and $203.82 \text{ m}^2 \text{ g}^{-1}$ for ZnS/SCNF-T4), together with an abundant tunneled-mesopore volume fraction of 83.32%, as summarized in Table 1, allowing the prediction of a radical improvement of the rate and ultrafast cycling capabilities for LIBs [13,28,29].

In order to characterize the morphology and inner structure further, we conducted a TEM analysis of the ZnS/SCNF-T3 sample. In Fig. 3a, the low-resolution TEM image shows the existence of dark spots within the CNF with diameters in the range of 195.98–201.78 nm and with transparent regions among them, indicating that NPs approximately 21.22–39.48 nm in size and tunneled mesopores in the approximate range of 29.63–43.41 nm are well dispersed over the CNF. In the enlarged TEM images (Fig. 3b and c), it was noted that the tunneled mesopores are located in the areas surrounding the ZnS NPs with a lattice fringe of 0.33 nm corresponding to the (100) plane of a wurtzite structure, which is evidence that the tunneled mesopores are formed by the sulfurization of the ZnO NPs to induce the oxidation reaction to the CNF in contact with the NPs. Furthermore, the elemental distribution of ZnS/SCNF-T3 as measured by EDS mapping (see Fig. 3d) clearly shows that Zn and S elements are uniformly dispersed along the CNF structure, indicating that the ZnS NPs are regularly embedded in the tunneled-mesopore CNF. These results prove that the hybrid nanocomposites of the tunneled-mesoporous SCNF embedded with the ZnS NPs are successfully fabricated during the sulfurization of the ZnO NPs induced by thiourea. This hybrid nanocomposite can accelerate the efficient transport of Li ions and electrons in the active materials for ultrafast LIB performance due to the shortened Li-ion diffusion pathway caused by the well-dispersed ZnS NPs in the tunneled-mesoporous CNF, the available space for the embedded ZnS NPs provided by the tunneled-mesoporous CNF structure, and the enhanced electrical conductivity caused by the S doping of the CNF [29].

To probe the variation of the crystal structure by the thiourea effect, we undertook a XRD analysis of the bare CNF, ZnS/SCNF-T2, ZnS/SCNF-T3, and ZnS/SCNF-T4 samples. As shown in Fig. 4a, all samples have in common broad peaks around 25.00° corresponding to the (002) plane of amorphous graphite. Unlike the bare CNF, the ZnS/SCNF-T2, ZnS/SCNF-T3, and ZnS/SCNF-T4 samples emit correspondingly sharp diffraction peaks at 26.93° , 28.52° , 30.55° , 47.60° , and 56.44° , providing strong evidence of the formation of the wurtzite ZnS phase with the (100), (002), (101), (110), and (112) planes (JCPDS card 36–1450), respectively, via the thiourea effect. However, ZnS/SCNF-T2 reveals a minor diffraction peak at 36.85° corresponding to the (002) plane of hexagonal Zn (JCPDS card,

87–0713) formed as a result of the reduction of the remaining ZnO during carbonization, which may indicate incomplete sulfurization due to the lack of the thiourea. These results are also confirmed by the Zn 2p XPS spectra (Fig. 4c). It was noted that the full width at half maximum (FWHM) of the ZnS peaks is distinguished among the samples. In addition, the grain sizes of the ZnS NPs (D_{ZnS}) were calculated using the Scherrer equation (Eq. (1)) [28]:

$$D_{\text{ZnS}} = 0.9 \lambda / (\beta \cdot \cos\theta) \quad (1)$$

where D_{ZnS} is the grain size of ZnS, λ is the wavelength of the X-rays, β is the FWHM, and θ is the Bragg angle. Based on the (100), (002), (101), (110), and (112) planes, the average grain sizes of the ZnS NPs are ~ 37.94 nm for ZnS/SCNF-T2, ~ 43.98 nm for ZnS/SCNF-T3, and ~ 50.61 nm for ZnS/SCNF-T4. Furthermore, TGA measurements were taken to investigate the ratio of the composed materials of all samples, as shown in Fig. 4b. Compared to showing the complete weight loss of bare CNF as a result of the burning of carbon, there is decreased weight loss from ZnS/SCNF-T2 (58.12%) to ZnS/SCNF-T4 (30.87%), which demonstrates that the tunneled-mesopore volume fraction was increased by the thiourea effect, burning the carbon during the sulfurization and S-doping steps, as shown in the BET results. To confirm the chemical bonding states of all of the samples, an XPS analysis is utilized. In the C 1s XPS spectra of all samples showing four characteristic peaks at approximately 284.5, 286.0, 287.6 and 288.9 eV corresponding to the C–C, C–O/C–N/C–S, C=O, and O–C=O bonding states (Fig. 4d), it was noted that the peak area ratio of C–O/C–N/C–S to C–C gradually increases from ZnS/SCNF-2 (0.38) to ZnS/SCNF-T4 (0.43), indicative of increased S-doping in the CNF [30,31]. The S 2p XPS spectra shown in Fig. 4e exhibit four characteristic peaks at approximately 161.2, 161.7, 162.9 and 163.7 eV corresponding to ZnS $2p_{3/2}$, ZnS $2p_{1/2}$, C–S–C $2p_{3/2}$, and C–S–C $2p_{1/2}$ for ZnS/SCNF-T2, ZnS/SCNF-T3, and ZnS/SCNF-T4, while there is no emission of the characteristic peaks by the bare CNF. Herein, the increased peak intensities of thiophenic-S from the bare CNF to ZnS/SCNF-T4 are indicative of an accelerated S-doping effect in the CNF once more, thus resulting in a gradual increase of the electrical conductivity of the electrodes (3.04 S cm^{-1} for bare CNF, 4.63 S cm^{-1} for ZnS/SCNF-T2, and 5.88 S cm^{-1} for ZnS/SCNF-T3), as the thiophenic-S with one S atom between two C atoms provides extra electrons by spin-orbit coupling, as shown in Fig. 4f [27]. In the Raman spectra, the ID/IG ratios of all samples gradually increased from 1.0 for bare-CNF to 1.09 for ZnS/SCNF-T4 without a band shift, as shown in Fig. S3. Because the formation of atomic defects due to C–C bonds are broken by the replaced S atoms, the order degree of the carbon structure is decreased [32,33]. However, despite the stronger S-doping effect for ZnS/SCNF-T4, the electrical conductivity (5.65 S cm^{-1}) of this sample is lower than that of the ZnS/SCNF-T3 sample, likely due to the discontinuous 1D structure induced by the excessive growth of ZnS NPs. Therefore, the hybrid nanocomposites of the tunneled-mesoporous SCNF embedded with the ZnS NPs fabricated with thiourea at 3 wt% have optimum electrical conductivity due to the synergic effect of the higher S-doping and the

Table 1

Specific surface area, total pore volume, average pore diameter, and pore volume fraction of the bare CNF, ZnS/SCNF-t2, ZnS/SCNF-t3, and ZnS/SCNF-t4 samples.

Samples	$S_{\text{BET}} [\text{m}^2 \text{ g}^{-1}]$	Total pore volume ($p/p_0 = 0.990$) [$\text{cm}^3 \text{ g}^{-1}$]	Average pore diameter [nm]	Pore volume fraction	
				$V_{\text{micro}} (\%)$	$V_{\text{meso}} (\%)$
Bare CNF	31.37	0.06	1.94	88.73	11.27
ZnS/SCNF-T2	82.68	0.21	5.20	52.16	47.84
ZnS/SCNF-T3	334.37	0.44	10.02	16.68	83.32
ZnS/SCNF-T4	203.82	0.32	6.33	34.64	65.36

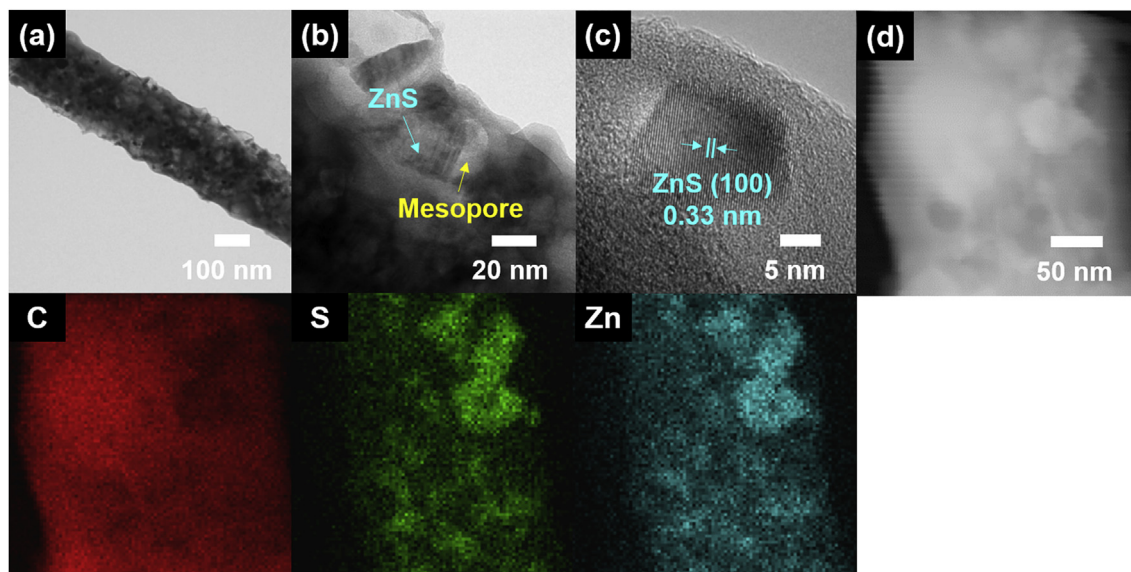


Fig. 3. (a) Low-resolution and (b and c) enlarged TEM images of ZnS/SCNF-T3, and (d) EDS mapping results of C, S, and Zn elements.

sophisticated 1D network structure of the CNF matrix, which clearly supports the accelerated ultrafast electrochemical performance outcomes [26,34].

The electrochemical performances of the LIBs are examined using galvanostatic charge/discharge tests. In Fig. 5a, the increased specific discharge capacities at the first cycle of the ZnS/SCNF electrodes compared to that of the bare CNF electrode are remarkable due to the participation of the ZnS NPs with a high theoretical specific capacity of 962.0 mAh g^{-1} (vs. 578.0 mAh g^{-1} for the bare CNF electrode) upon the electrochemical reaction [10]. Compared to the other ZnS/SCNF electrodes ($1457.9 \text{ mAh g}^{-1}$ for ZnS/SCNF-T2 and $1012.0 \text{ mAh g}^{-1}$ for ZnS/SCNF-T4), the ZnS/SCNF-T3 electrode is shown to deliver higher specific discharge capacities ($1627.2 \text{ mAh g}^{-1}$) at the first cycle. This stems from the optimized thiourea effect to induce the complete formation of ZnS NPs in the CNF without excessive NP growth, as confirmed by the SEM (Fig. 2) and XRD results (Fig. 4a). The galvanostatic charge/discharge voltage profiles clearly produce definite two voltage plateaus in the discharge process of the first cycle at 0.75 V, attributed to the reduced reaction of the ZnS ($\text{ZnS} + \text{Li}^+ + 4\text{e}^- \rightarrow \text{Li}_2\text{S} + \text{Zn}$) in the voltage range of 0.01–0.4 V, corresponding to the further sequential lithiation reaction of Zn to form the LiZn phase ($\text{Zn} \rightarrow \text{LiZn}_4 \rightarrow \text{LiZn}$) and contributing to SEI layer formation at the ZnS NPs to cause an irreversible capacity and low Coulombic efficiency (41.3% for the bare CNF electrode, 46.8% for the ZnS/SCNF-T2 electrode, 51.9% for the ZnS/SCNF-T3 electrode, and 47.1% for the ZnS/SCNF-T4 electrode), as previously reported [35,36]. Among these, the initial Coulombic efficiency of ZnS/SCNF-T3 shows the highest value, possibly due to the internal construction of the tunneled-mesoporous CNF structure, which enhances the efficient Li-ion transport of the ZnS NPs [37–39]. With reversible operation of the electrochemical behavior of all electrodes after reaching 100.0% Coulombic efficiency at eight cycles, the ZnS/SCNF-T3 electrode shows superb cycling retention (90.7%) with a high discharge capacity of 654.2 mAh g^{-1} after 100 cycles compared to the ZnS/SCNF-T2 electrode (89.7% with 497.4 mAh g^{-1}) and the ZnS/SCNF-T4 electrode (85.8% with 427.9 mAh g^{-1}). This performance outcome indicates that the optimized tunneled-mesoporous 1D structure with a superb specific surface area very is highly effectively improves the electrochemical stability due to the provision of

available space for the extensive volume change of the ZnS NPs during the Li-ion charge/discharge process. Fig. 5b presents the rate performance outcomes of LIBs acquired at various current densities from 100 to 2000 mA g^{-1} and then at 100 mA g^{-1} . When the applied current density is gradually increased from 100 to 2000 mA g^{-1} , the capacity retention of the ZnS/SCNF-T3 electrode (63.2%) is best compared to those of the bare CNF (34.1%), ZnS/SCNF-T2 (53.9%) and ZnS/SCNF-T4 electrodes (39.8%). When the current density returns to 100 mA g^{-1} , the ZnS/SCNF-T3 electrode also shows strong reversibility with a discharge capacity of 97.2% at the original 100 mA g^{-1} in comparison with the other electrodes (94.7% for the bare CNF electrode, 95.1% for the ZnS/SCNF-T2 electrode, and 80.5% for the ZnS/SCNF-T4 electrode). The amazing rate capability of the ZnS/SCNF-T3 electrode can be ascribed to the efficient transport of Li ions and electrons via the hybrid nanocomposites composed of well-dispersed ZnS NPs and the tunneled-mesoporous structure of the SCNF, even showing an outstanding value of an ultrafast current density of 2000 mA g^{-1} compared to those of ZnS-based composites reported previously (see Fig. 5d) [40–45]. In addition, this may be expandable to ultrafast cycling performance at a high current density of 2000 mA g^{-1} for LIBs used in practical products, as shown in Fig. 5c. After 500 cycles, compared to the other electrodes (86.3% for the ZnS/SCNF-T2 electrode and 51.9% for the ZnS/SCNF-T4 electrode), the ZnS/SCNF-T3 electrode displays remarkable ultrafast performance in the form of stable cycling retention of 97.2% with a high specific capacity of 391.8 mAh g^{-1} . The excellent ultrafast cycling capability is attributed to the synergistic effects in the hybrid nanocomposites via the thiourea, i.e., the formation of complete ZnS NPs in the CNF matrix to realize the high specific capacity, the internal construction of the tunneled-mesoporous CNF structure to provide available space for the volume expansion of the embedded ZnS NPs during the Li-ion charge/discharge process and efficient Li-ion diffusion, and the improvement of the electrical conductivity by the S doping in the CNF matrix to accelerate the electrochemical kinetics of the electrode. Additionally, we undertook the quantification of the capacitive behavior (k_1v) and diffusion control ($k_2v^{1/2}$) capacitance using the CV curves with various scan rates (v) corresponding to 2, 3, 5, 7, and 10 mV s^{-1} (Eq. (2)) [38,39].

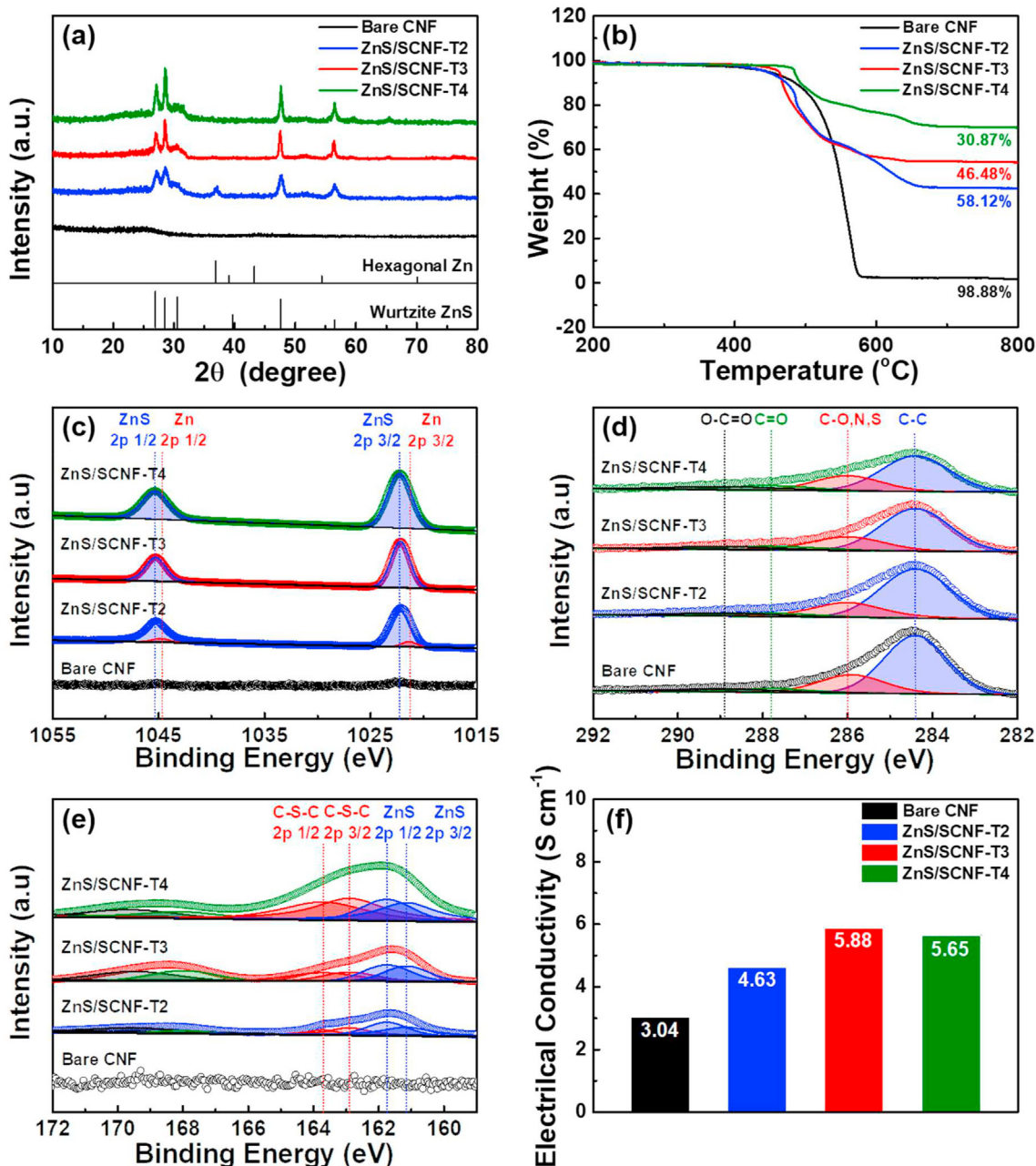


Fig. 4. (a) XRD patterns, (b) TGA curves, and XPS spectra of (c) C 1s, (d) S 2p, and (e) Zn 2p, and (f) electrical conductivity results of the bare CNF, ZnS/SCNF-T2, ZnS/SCNF-T3, and ZnS/SCNF-T4 samples.

$$i(V) = k_1v + k_2v^{1/2} \quad (2)$$

As shown in Fig. S3c, the pseudocapacitive contribution of ZnS/SCNF-T3 exceeds that of the bare CNF with an increase in the scan rate, which may be related to effect of the tunneled-mesoporous structure with efficient ion diffusion pathways and S-doped CNF with increased electrical conductivity to accelerate the electrochemical double-reaction of Li ions and electrons into the ZnS NPs. This result can function as a potential factor in the improved ultrafast capability [38,39]. To confirm the electrochemical kinetics regarding Li-ion diffusion for the hybrid nanocomposites, EIS measurements were taken. In Fig. 5e, the lower charge transfer resistance (R_{ct}) of the ZnS/SCNF-T3 electrode compared to the other samples is readily apparent, and the R_{ct} value in this case remains

unchanged after ultrafast cycling of 500 cycles (see Table S1); this is directly related to the superb electrical conductivity of the electrodes together with the fastest Li-ion diffusion rate, also proved by the Warburg impedance coefficients (σ_w), as the Warburg impedance was estimated using sloping lines in the low-frequency range according to the following equations (Eqs. (3–4)) [26,27,46–49],

$$Z_{real} = R_e + R_{ct} + \sigma_w \omega^{-1/2} \quad (3)$$

$$D_{Li} = R^2 T^2 / 2A^2 n^4 F^4 C^2 \sigma_w \quad (4)$$

where D_{Li} is the Li-ion diffusion coefficient, R is the gas constant, T is the temperature, F is the Faraday constant, and C is the molar concentration. In the relationship between $\omega^{-1/2}$ and Z_{real} , the

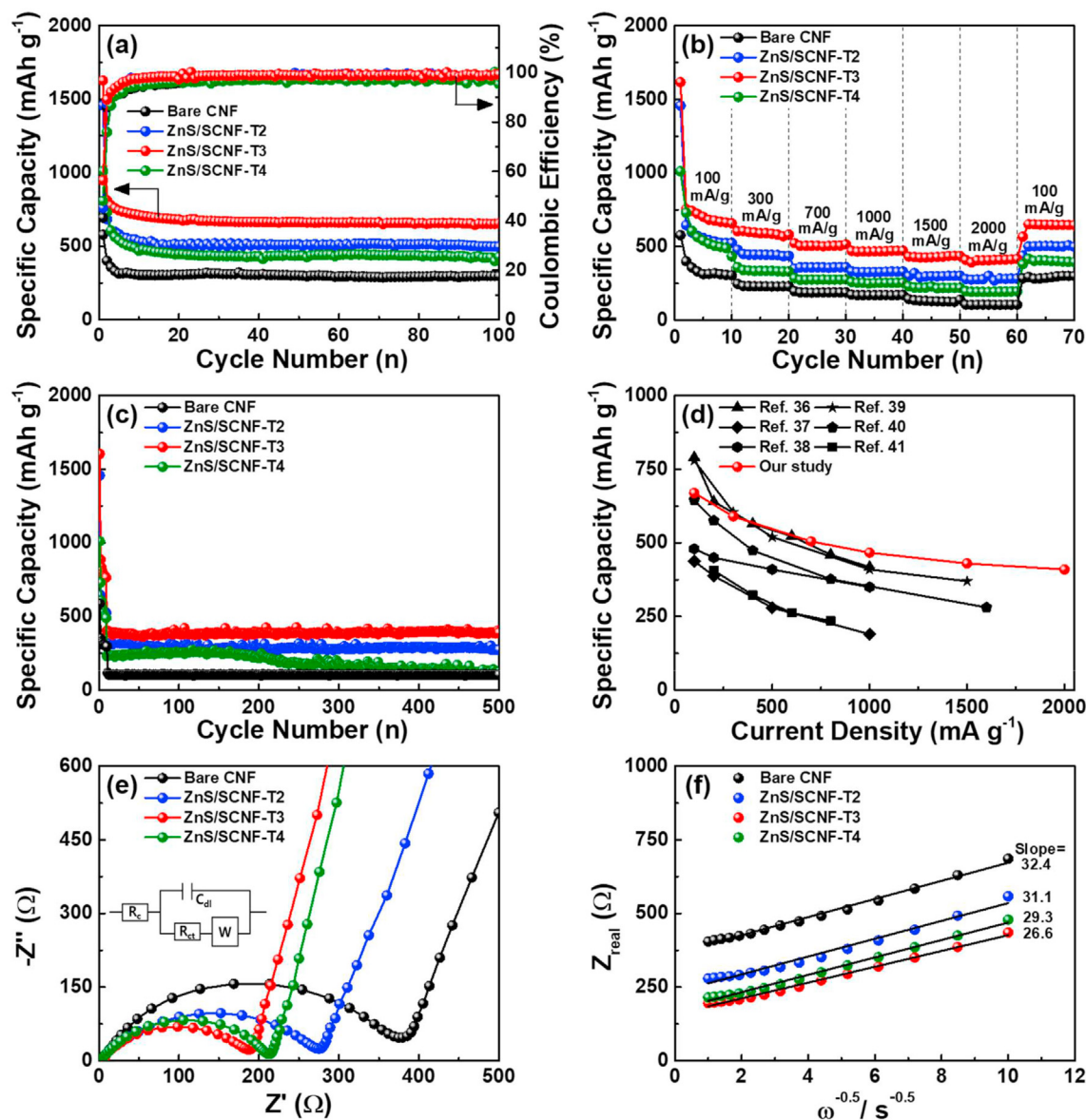


Fig. 5. (a) Cycling performance, (d) rate performance, and (c) ultrafast cycling capability of the bare CNF, ZnS/SCNF-T2, ZnS/SCNF-T3, and ZnS/SCNF-T4 electrodes, (d) comparative plots of the rate performance capability of the ZnS/SCNF-T3 electrode with the ZnS-based composite electrode for LIBs reported previously, and (e) Nyquist plots of all samples obtained in the low frequency range at the open-circuit voltage.

obtained σ_w values for the bare CNF, ZnS/SCNF-T2, ZnS/SCNF-T3, and ZnS/SCNF-T4 electrodes are 32.4, 31.1, 26.6, and 29.3 $\Omega\text{cm}^2\text{s}^{-1/2}$, respectively. The value of the Li-ion diffusion coefficient as calculated from σ_w is 3.0×10^{-13} for the bare CNF electrode, 3.6×10^{-13} for the ZnS/SCNF-T2 electrode, 4.8×10^{-13} for the ZnS/SCNF-T3 electrode, and 4.0×10^{-13} cm^2s^{-1} for the ZnS/SCNF-T4 electrode, confirming that the Li-ion diffusion coefficient of the ZnS/SCNF-T3 electrode shows the best value and indicating the decreasing reactive resistance of the Li ions and electrons of the electrode itself during the ultrafast electrochemical reaction. Therefore, the hybrid nanocomposites of tunneled-mesoporous SCNF embedded with the ZnS NPs can be suggested as a potential candidate to accelerate the ultrafast cycling performance of LIBs.

4. Conclusion

In summary, we developed unique hybrid nanocomposites of tunneled-mesoporous SCNF embedded with ZnS NPs through a

one-pot carbonization process using the thiourea effect. During carbonization, the thermal decomposition of the thiourea induced the sulfurization of the ZnO NPs in the CNF due to the chemical reaction with the formed H_2S , which played important roles in the formation of the tunneled mesopores and in S-doping over the CNF embedded with the ZnS NPs. Upon the optimization of the thiourea effect during the carbonization process, the hybrid nanocomposites fabricated with 3 wt% thiourea (ZnS/SCNF-T3) presented a tunneled-mesoporous CNF structure with a superb specific surface area and well-dispersed ZnS NPs internally. This also provided available space for the abrupt volume expansion of the ZnS NPs with a high specific capacity and efficient Li-ion diffusion during the electrochemical reactions. As a result, the ZnS/SCNF-T3 demonstrates competitive and superb cycling retention (90.6% with a high discharge capacity of 654.2 mAh g^{-1} after 100 cycles) and stable rate capability compared to the other samples. In addition, even at an ultrafast current density (2000 mA g^{-1}), the reversible specific capacity reached 391.8 mAh g^{-1} with sustained cycling

stability of 97.2% after 500 cycles, mainly due to the combined effects of the three unique characteristics of the hybrid nanocomposites, i.e., the desirable discharge capacity caused by the well-dispersed ZnS NPs in the CNF matrix and the available space for volume expansion of the embedded ZnS NPs, the shortened Li-ion diffusion pathway of the ZnS NPs due to the internal construction of the tunneled-mesoporous CNF structure, as well as the accelerated electrical conductivity of the electrode by the S doping effect of the CNF matrix. Therefore, the novel construction of the unique hybrid nanocomposites presented here offers a potential approach by which to develop an effective anode material using ZnS for improving the ultrafast Li storage capabilities of LIBs.

CRedit authorship contribution statement

Ki-Wook Sung: Conceptualization, Methodology, Investigation, Writing - review & editing. **Bon-Ryul Koo:** Methodology. **Hyo-Jin Ahn:** Conceptualization, Supervision, Writing - review & editing.

Declaration of competing interest

The authors declare that they have no known competing financial interests or personal relationships that could have appeared to influence the work reported in this paper.

Acknowledgments

This work was supported by a the National Research Foundation of Korea (NRF) grant funded by the Korea government (MSIT) (No. 2019R1 A2 C1005836).

Appendix A. Supplementary data

Supplementary data to this article can be found online at <https://doi.org/10.1016/j.jallcom.2020.157206>.

References

- 1] M. Armand, J.-M. Tarascon, Building better batteries, *Nature* 451 (2008) 652–657.
- 2] P.G. Bruce, B. Scrosati, J.-M. Tarascon, Nanomaterials for rechargeable lithium batteries, *Angew. Chem. Int. Ed.* 47 (2008) 2930–2946.
- 3] C. Laing, M. Hao, H. Pan, Y. Liu, M. Yan, Lithium alloys and metal oxides as high-capacity anode materials for lithium-ion batteries, *J. Alloys Compd.* 575 (2013) 246–256.
- 4] G.-H. An, D.-Y. Lee, H.-J. Ahn, Carbon-Encapsulated hollow porous vanadium-oxide nanofibers for improved lithium storage properties, *ACS Appl. Mater. Interfaces* 8 (2016) 19466–19474.
- 5] G.-H. An, D.-Y. Lee, Y.-J. Lee, H.-J. Ahn, Ultrafast lithium storage using antimony-doped tin oxide nanoparticles sandwiched between carbon nanofibers and a carbon skin, *ACS Appl. Mater. Interfaces* 8 (2016) 30264–30270.
- 6] F. Zhang, T. Zhang, X. Yang, L. Zhang, K. Leng, Y. Huang, Y. Chen, A high-performance supercapacitor-battery hybrid energy storage device based on graphene-enhanced electrode materials with ultrahigh energy density, *Energy Environ. Sci.* 6 (2013) 1623–1632.
- 7] P.K. Nayak, L. Yang, W. Brehm, P. Adelhelm, From lithium-ion to sodium-ion batteries: advantages, challenges, and surprises, *Angew. Chem. Int. Ed.* 57 (2018) 102–120.
- 8] G.-H. An, J.I. Sohn, H.-J. Ahn, Hierarchical architecture of hybrid carbon-encapsulated hollow manganese oxide nanotubes with a porous-wall structure for high-performance electrochemical energy storage, *J. Mater. Chem.* 4 (2016) 2049–2054.
- 9] G.-H. An, H. Kim, H.-J. Ahn, Excavated carbon with embedded Si nanoparticles for ultrafast lithium storage, *J. Ind. Eng. Chem.* 68 (2018) 146–152.
- 10] X. Du, H. Zhao, Y. Lu, Z. Zhang, A. Kulka, K. Świerczek, Synthesis of core-shell like ZnS/C nanocomposite as improved anode material for lithium ion batteries, *Electrochim. Acta* 228 (2017) 100–106.
- 11] Y.S. Jang, Y.C. Kang, Facile one-pot synthesis of spherical zinc sulfide-carbon nanocomposite powders with superior electrochemical properties as anode materials for Li-ion batteries, *Phys. Chem. Chem. Phys.* 15 (2013) 16437–16441.
- 12] H. Ren, Z. Wen, G. Wu, S. Chen, S.W. Joo, J. Huang, Preparation of zinc sulfide@reduced graphene oxide nanocomposites with enhanced energy storage performance, *J. Phys. Chem. Solid.* 134 (2019) 43–51.
- 13] R. Zhang, Y. Wang, M. Jia, J. Xu, E. Pan, One-pot hydrothermal synthesis of ZnS quantum dots/graphene hybrids as a dual anode for sodium ion and lithium ion batteries, *Appl. Surf. Sci.* 437 (2018) 375–383.
- 14] F.-S. Ke, Y.-S. Wu, H. Deng, Metal-organic frameworks for lithium ion batteries and supercapacitors, *J. Solid State Chem.* 223 (2015) 109–121.
- 15] L. Wang, J. Ju, N. Deng, G. Wang, B. Cheng, ZnS nanoparticles anchored on porous carbon nanofibers as anode materials for lithium ion batteries, *Electrochim. Commun.* 96 (2018) 1–5.
- 16] Z. Xu, Z. Zhang, M. Li, H. Yin, H. Lin, J. Zhou, S. Zhou, Three-dimensional ZnS/reduced graphene oxide/polypyrrole composite for high-performance supercapacitors and lithium-ion battery electrode material, *J. Solid State Chem.* 23 (2019) 3419–3428.
- 17] J. Yoon, I.T. Kim, J. Bae, J. Hur, High-performance ZnS@graphite composites prepared through scalable high-energy ball milling as novel anodes in lithium-ion batteries, *J. Ind. Eng. Chem.* 76 (2019) 258–267.
- 18] H. Wu, G. Li, Y. Li, Z. Geng, T. Ren, T. Cai, Z. Yang, Synthesis of ZnS/C composites by metal-organic framework as high-performance lithium-ion batteries, *Cryst. Res. Technol.* 54 (No) (2019) 1–5, 1800281.
- 19] Z. Chen, R. Wu, H. Wang, Y. Jiang, L. Jin, Y. Guo, Y. Song, F. Fang, D. Sun, Construction of hybrid hollow architectures by in-situ rooting ultrafine ZnS nanorods within porous carbon polyhedra for enhanced lithium storage properties, *Chem. Eng. J.* 326 (2017) 680–690.
- 20] J. Li, D. Yan, X. Zhang, S. Hou, T. Ku, Y. Yao, L. Pan, ZnS nanoparticles decorated on nitrogen-doped porous carbon polyhedra: a promising anode material for lithium-ion and sodium-ion batteries, *J. Mater. Chem.* 5 (2017) 20428–20439.
- 21] M. Ohta, S. Hirai, H. Kato, V.V. Sokolov, V.V. Bakovets, Thermal decomposition of NH₄SCN for preparation of Ln₂S₃ (Ln = La and Gd) by sulfurization, *Mater. Trans.* 50 (No. 7) (2009) 1885–1889.
- 22] E. Karami, M. Tavoosi, A. Ghasemi, G.R. Gordani, Evaluation of diffusion mechanism and structural characterizations of ZnS compound during chemical reaction of Zn and S in liquid phase, *J. Sulfur Chem.* 39 (No. 5) (2018) 495–506.
- 23] R. Zhang, B. Wang, H. Zhang, L. Wei, Influence of sulfidation ambience on the properties of nanocrystalline ZnS films prepared by sulfurizing the as-sputtered ZnO films, *Appl. Surf. Sci.* 245 (2005) 340–345.
- 24] M. Seredych, M. Khine, T.J. Bandosz, Enhancement in dibenzothiophene reactive adsorption from liquid fuel via incorporation of sulfur heteroatoms into the nanoporous carbon matrix, *ChemSuschem* 4 (2011) 139–147.
- 25] N. Galland, F. Caralp, M.-T. Rayez, Y. Hannachi, J.-C. Loison, G. Dorthé, A. Bergeat, Reaction of carbon atoms, C (2p², 3P), with hydrogen sulfide, H₂S (X¹A₁): Overall rate constant and product channels, *J. J. Phys. Chem. A* 105 (2001) 9893–9900.
- 26] D.-Yo Shin, H.-G. Jo, H.-J. Ahn, Accelerating lithium storage capability of cobalt sulfide encapsulated within anion dual-doped mesoporous carbon nanofibers, *Appl. Surf. Sci.* 527 (2020) 146895, 145904.
- 27] X. Shen, D. Mu, S. Chen, B. Wu, F. Wu, Enhanced electrochemical performance of ZnO-Loaded/Porous carbon composite as anode materials for lithium ion batteries, *ACS Appl. Mater. Interfaces* 5 (2013) 3118–3125.
- 28] G.-H. An, H.-J. Ahn, Ultrafast lithium storage of high dispersed silicon and titanium oxide nanoparticles in carbon, *J. Alloys Compd.* 710 (2017) 274–280.
- 29] B.-R. Koo, H. An, H.-J. Ahn, High-surface area electrospun TiO₂ nanowires fabricated using shrinkage of polyvinylpyrrolidone for improved photovoltaic performance, *Ceram. Int.* 42 (2016) 1666–1671.
- 30] Q. Xu, P. Pu, Z. Zhao, C. Dong, C. Gao, Y. Chen, J. Chen, Y. Kiu, H. Zhou, Preparation of highly photoluminescent sulfur-doped carbon dots for Fe(III) detection, *J. Mater. Chem.* 3 (3) (2015) 542–546.
- 31] W. Si, J. Zhou, S. Zhang, S. Ki, W. Xing, S. Zhou, Tunable N-doped or dual N, S-doped activated hydrothermal carbons derived from human hair and glucose for supercapacitor applications, *Electrochim. Acta* 107 (2013) 397–405.
- 32] Y. Wang, S. Serrano, J.J. S-Aviles, Raman characterization of carbon nanofibers prepared using electrospinning 138 (2003) 423–427.
- 33] Y. Liu, C. Pan, J. Wang, Raman Spectra of Carbon Nanotubes and Nanofibers Prepared by Ethanol Flames, vol. 39, 2004, pp. 1091–1094.
- 34] W. Li, M. Zhou, H. Li, K. Wang, S. Cheng, K. Jiang, A high performance sulfur-doped disordered carbon anode for sodium ion batteries, *Energy Environ. Sci.* 8 (2015) 2916–2921.
- 35] Q.H. Nguyen, T. Park, J. Hur, Enhanced cycle stability of zinc sulfide anode for high-performance lithium-ion storage: Effect of conductive hybrid matrix on active ZnS, *Nanomaterials* 9 (2019) 1221–1235.
- 36] G. Tian, Z. Zhao, A. Sarapulova, C. Das, L. Zhu, S. Liu, A. Missiul, E. Welter, J. Maibach, S. Dsoke, Understanding the Li-ion storage mechanism in a carbon composited zinc sulfide electrode, *J. Mater. Chem.* 7 (2019) 15640–15653.
- 37] B.-R. Koo, M.-H. Jo, K.-H. Kim, H.-J. Ahn, Multifunctional electrochromic energy storage devices by chemical cross-linking: impact of a WO₃·H₂O nanoparticle-embedded chitosan thin film on amorphous WO₃ films, *NPG Asia Mater.* 12 (No. 10) (2012) 1–12.
- 38] B.-R. Koo, K.-W. Sung, H.-J. Ahn, Boosting ultrafast lithium storage capability of hierarchical core/shell constructed carbon nanofiber/3D interconnected hybrid network with nanocarbon and FTO nanoparticle heterostructures, *Adv. Funct. Mater.* (2020) 1–11, 2001863.
- 39] E. Lim, C. Jo, H. Kim, M.-H. Kim, Y. Mun, J. Chun, Y. Ye, J. Hwang, K.-S. Ha, K.C. Roh, K. Kang, S. Yoon, J. Lee, Facile synthesis of Nb₂O₅@carbon core-shell nanocrystals with controlled crystalline structure for high-power anodes in hybrid supercapacitors, *ACS Nano* 9 (2015) 7497–7505.

- [40] M. Chen, B. Li, X. Liu, L. Zhou, L. Yao, J. Jai, X. Qian, X. Yu, Boron-doped porous Si anode materials with high initial coulombic efficiency and long cycling stability, *J. Mater. Chem.* 6 (2018) 3022–3027.
- [41] L. He, X.-Z. Liao, K. Yang, Y.-S. He, W. Wen, Z.-F. Ma, Electrochemical characteristics and intercalation mechanism of ZnS/C composite as anode active material for lithium-ion batteries, *Electrochim. Acta* 56 (2011) 1213–1218.
- [42] M. Mao, L. Jiang, L. Wu, M. Zhang, T. Wang, The structure control of ZnS/graphene composites and their excellent properties for lithium-ion batteries, *J. Mater. Chem.* 3 (2015) 13384–13390.
- [43] Y. Fu, Z. Zhang, X. Yang, Y. Gan, W. Chen, ZnS nanoparticles embedded in porous carbon matrices as anode materials for lithium ion batteries, *RSC Adv.* 8 (2015) 86941–86945.
- [44] J. Li, Y. Fu, X. Shi, Z. Xu, Z. Zhang, Urchinlike ZnS microspheres decorated with nitrogen-doped carbon: a superior anode material for lithium and sodium storage, *Chem. Eur J.* 23 (2017) 157–166.
- [45] H. Chen, B. Zhang, Y. Gao, X. Wang, Y. Yao, W. Yu, J. Zheng, J. Zhang, H. Tong, ZnS nanoparticles embedded in porous honeycomb-like carbon nanosheets as high performance anode material for lithium ion batteries, *Ceram. Int.* 44 (2018) 13706–13711.
- [46] J. Ma, X. Wang, H. Wang, G. Wang, S. Ma, Hollow ZnS microspheres encapsulated in carbon shells with enhanced lithium and sodium storage properties, *J. Alloys Compd.* 735 (2018) 51–61.
- [47] X. Li, K. Zhang, D. Mitlin, E. Paek, M. Wang, F. Jiang, Y. Huang, Z. Yang, Y. Gong, L. Gu, W. Zhao, Y. Du, J. Zheng, Li-Rich $\text{Li}[\text{Li}_{1/6}\text{Fe}_{1/6}\text{Ni}_{1/6}\text{Mn}_{1/2}]\text{O}_2$ (LFNMO) cathodes: atomic scale insight on the mechanisms of cycling decay and of the improvement due to cobalt phosphate surface modification, *Small* 14 (No. 1802570) (2018) 1–12.
- [48] X. Li, K. Zhang, D. Mitlin, Z. Yang, M. Wang, Y. Tang, F. Jiang, Y. Du, J. Zheng, Fundamental insight into Zr modification of Li- and Mn-rich cathodes: combined transmission electron microscopy and electrochemical impedance spectroscopy study, *Chem. Mater.* 30 (2018) 2566–2573.
- [49] X. Li, J. Zheng, X. Ren, M.H. Engelhard, W. Zhao, Q. Li, J.-G. Zhang, W. Xu, Dendrite-free and performance-enhanced lithium metal batteries through optimizing solvent compositions and adding combinational additives, *Adv. Energy. Mater.* 1703022 (2018) 1–10.